

Microstructure and Mechanical Properties of 21-6-9 Stainless Steel Electron Beam Welds



JOHN W. ELMER, G. FRED ELLSWORTH, JEFFREY N. FLORANDO, ILYA V. GOLOSKER, and RUPALEE P. MULAY

Welds can either be stronger or weaker than the base metals that they join depending on the microstructures that form in the fusion and heat-affected zones of the weld. In this paper, weld strengthening in the fusion zone of annealed 21-6-9 stainless steel is investigated using cross-weld tensile samples, hardness testing, and microstructural characterization. Due to the stronger nature of the weld, the cross-weld tensile tests failed in the base metal and were not able to generate true fusion zone mechanical properties. Nanoindentation with a spherical indenter was instead used to predict the tensile behavior for the weld metal. Extrapolation of the nanoindentation results to higher strains was performed using the Steinberg–Guinan and Johnson–Cook strength models, and the results can be used for weld strength modeling purposes. The results illustrate how microstructural refinement and residual ferrite formation in the weld fusion zone can be an effective strengthener for 21-6-9 stainless steel.

DOI: 10.1007/s11661-017-3996-y

© The Minerals, Metals & Materials Society and ASM International (outside the USA) 2017

I. INTRODUCTION

ELECTRON beam (EB) welds in annealed 21-6-9 stainless steel (SS) sheet were made and characterized to determine the weld fusion zone (FZ) and base metal mechanical properties for use in structural design calculations. Alloy 21-6-9 SS, also known as Nitronic 40, was developed as an improved austenitic stainless steel over traditional 300 series stainless steel alloys. This alloy contains nominally 21 pct Cr, 6 pct Ni, 9 pct Mn (compositions in wt pct) and has improved corrosion resistance due to its higher Cr content of 21 pct. In addition, 21-6-9 SS uses N rather than C as a strengthener, which reduces the tendency for corrosion sensitization that can occur during heat treating and welding. Nitrogen can be added up to 0.35 pct, which improves the room temperature yield strength of 21-6-9 SS over 300 series stainless steel alloys, while maintaining good toughness and high ductility (>40 pct elongation to failure). Manganese is added to 21-6-9 SS to increase austenite stability, particularly at cryogenic temperatures, while reducing the Ni content from 8 to 6 pct as compared to 300 series stainless steels. 21-6-9 SS can be further strengthened by cold work and can be machined, forged, and welded using the same methods as 300-series stainless steels. A review report on characterization of 21-6-9 SS base metal can be found in Reference 1, and its yield stress over a wide range of strain rates and temperatures can be found in Kassner and Breithaup.^[2]

Although the base metal properties of 21-6-9 SS are well documented, the properties of the welds are not as well understood. Measuring the mechanical properties of weld joints is complicated by the fact that microstructure and property gradients are formed in the weld FZ and heat-affected zone (HAZ) due to the localized nature of welding heat sources. Oftentimes, the welds are not large enough to allow the extraction of all-weld metal tensile bars from the FZ, and under these circumstances cross-weld tensile bars are sometimes used. The cross-weld tensile samples give an overall measure of the joint performance and fail in the weakest portion of the weld joint region, which may be the base metal, HAZ or FZ depending on the material and the welding conditions. In order to measure the mechanical properties of the weld FZ itself, hardness measurements are often performed and sometimes correlated with stress–strain behavior using microhardness and nanoindentation methods.^[3,4]

This study characterizes EB welds tested in a cross-weld geometry with different sample sizes and configurations, and the results are compared to a nanoindentation method for predicting stress–strain behavior. The results are modeled using the Steinberg–Guinan and Johnson–Cook models^[5,6] to create mechanical property data for 21-6-9 SS welds over a wide range of strains under quasi-static conditions at room temperature.

II. MATERIAL AND EXPERIMENTAL PROCEDURES

A. Materials

Annealed 21-6-9 SS plate was acquired with the composition summarized in Table I, where the

JOHN W. ELMER, G. FRED ELLSWORTH, JEFFREY N. FLORANDO, ILYA V. GOLOSKER, and RUPALEE P. MULAY are with the Lawrence Livermore National Laboratory, Livermore, CA, 94550. Contact e-mail: elmer1@llnl.gov

Manuscript submitted February 6, 2016.

Article published online February 7, 2017

measured “actual” composition of the plate is compared to the commercial specification and the desired target composition range for weldability. The target alloy composition has a lowered nitrogen content compared to the standard specification to improve electron beam weldability. The initial plate measured 3 mm thick and was further machined to the size of 100 × 200 × 1.5 mm for welding and mechanical property testing. Ferrite measurements were made on the base metal using a Magne-Gage tester and a number 3 magnet, which is used for measuring ferrite in austenitic stainless steels, and shows that the base metal had no measurable ferrite. After welding, the ferrite content was measured on polished cross sections and on the top of the electron beam weld beads, showing that the welds contained delta ferrite that measured between 0.8 to 1.1 pct. However, due to the small weld volume (~1 mm deep, 1.5 mm wide), the magnetic measurements underestimate the actual ferrite content of the weld by as much as 5× due to the incorporation of the zero percent base metal ferrite into the readings.^[7]

B. Electron Beam Welding

Samples to be welded were machined to the size of 50 × 200 × 1.5 mm, so that when welded along their length they would have the same dimensions as the base metal samples. The weld joint preparation was a step joint configuration, which has a step height requiring 1 mm weld penetration. Electron beam welds were made using a Hamilton Standard 605 electron beam welder at LLNL. All welds were made with a 9 inch work distance and performed at 4×10^{-5} Torr vacuum. The Enhanced Modified Faraday Cup (EMFC) electron beam diagnostic was used to measure the properties (peak power density, full-width half-maximum, beam diameter, and beam aspect ratio) of each beam prior to welding, as summarized in Table II, using the method detailed elsewhere.^[8]

C. Tensile Testing

The base metal and welded plates were electro discharge machined (EDM) into two different sized tensile bars as illustrated in Figure 1. The “regular” tensile bars measured 102 mm long, and are based on an ASTM E-8 tensile sample with a length-to-width ratio of 4:1. The “mini” tensile samples were 2/5 size and

maintained the same 4:1 length-to-width ratio. Tensile bars removed from the welded plate are cross-weld tensile samples, since all-weld, longitudinal, tensile bars were not able to be prepared due to the small volume of welded material. The welded tensile samples were further prepared using two methods as illustrated in Figure 2(a). The first method used the tensile bar in the full-thickness (1.5 mm) as-welded condition, *i.e.*, with an unwelded portion of joint directly below the step joint (see Figure 2(b)). The second method prepared the welds by machining the top and bottom surfaces of the welded sample to a final thickness of 0.75 mm so as to remove any weld reinforcement and undercut on the top surface and the unwelded portion below the step (see Figure 2(c)). Cross sectional areas of the samples were measured on the welded portion of this sample, to calculate the stress on each sample to account for any variations in machining that may have occurred.

The “mini” sample tests were performed in an Instron 4444 electromechanical test machine at room temperature and position control at a rate of .508 mm/minute. A strain extensometer with a gage length of 5.715 mm—50 pct was used to measure the strain for the base and milled weld mini tensile samples, while a 0.138 inch gage length was used on the full-thickness mini samples. In all cases the knife edges of the extensometer were located across the width of the sample and centered over the weld. The “regular sample” tests were performed in an Instron 5800R/4505 test machine at room temperature and position control at a rate of 0.050 in/minute. An EIR LE-01 laser extensometer with a 25.4 mm gage length was used to measure strain for the regular-sized samples, with the gage length centered over the weld, and with the laser facing the top (weld side) of the sample. The laser measured the extension of two dimples on the sample that defined the gage length. The modulus of elasticity was determined by the best fit straight line through the linear portion of the stress–strain curve, the yield strength was determined using a 0.2 pct offset method, and the ultimate tensile strength was determined by the peak load divided by the load bearing area at the thinnest portion of the step joint sample configuration.

D. Microstructure, Microhardness, and Nanoindentation Testing

Metallographic cross sections of the welds and base metals were performed using standard preparation

Table I. 21-6-9 Stainless Steel Alloy Composition Compared to Nominal and LLNL Aim Ranges for Electron Beam Weldability

Element	Actual (Wt Pct)	Specification (Wt Pct)	LLNL Aim (Wt Pct)
Carbon	0.02	0.08 max	0.04 max
Chromium	19.96	19.0 to 21.5	20 to 20.5
Nickel	7.02	5.5 to 7.5	6.0 to 6.5
Manganese	9.14	8.0 to 10.0	8.5 to 9.5
Silicon	0.05	1.0 max	0.50 max
Nitrogen	0.23	0.15 to 0.40	0.23 to 0.25
Phosphorous	0.014	0.06 max	0.000
Sulfur	<0.005	0.03 max	0.000
Oxygen	<0.001	—	0.000 to 0.005
Iron	balance	balance	balance

Table II. Summary of the electron Beam Properties for Each of the Six Welds, Along with the Resulting Weld Depths and Widths Across the Top Surface of the Plate

Weld	Focus Setting (mA)	Peak Power Density (W/mm ²)	FWHM (mm)	Beam Diameter (mm)	Weld Depth (mm)	Weld Width (mm)
1	762 (+ 32)	1500	0.49	0.98	0.98	1.53
2	760 (+ 30)	1550	0.51	0.97	1.03	1.52
3	760 (+ 30)	1510	0.51	0.98	1.11	1.56
4	759 (+ 29)	1480	0.54	1.00	1.14	1.55
5	759 (+ 29)	1445	0.52	1.01	1.00	1.53
6	759 (+ 29)	1470	0.51	0.99	0.99	1.51
Avg./STD	759.8/1.2	1493/36.2	0.51/.02	0.99/.02	1.04/.07	1.53/.02

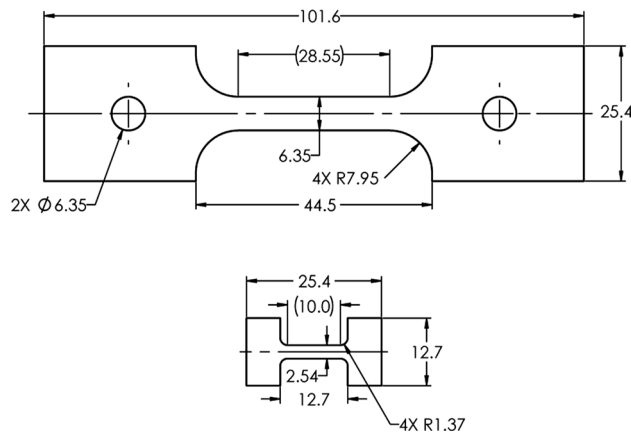


Fig. 1—Drawings of the regular size (top) and mini (bottom) base metal tensile bars with dimensions in mm. Cross-weld samples were prepared from two welded sheets with the weld running across the center of the gage length and perpendicular to the tensile bar axis.

procedures. The samples were sectioned on a slow speed diamond saw, potted in a clear two-part epoxy, and then ground on successive silicon carbide papers from 320 to 2400 grit. The samples were polished first using 3 μm diamond paste, followed by a 1 μm alumina slurry. The samples were electrolytically etched in a 5 to 10 pct oxalic acid solution at room temperature to bring out the microstructure. Macro photographs of the entire weld fusion zone shapes were made using a Keyence VHX-600E digital microscope, while higher magnification micrographs were made using a Reichert inverted stage metallograph.

The electroetched samples were used for electron-backscattered diffraction (EBSD). EBSD was carried out using two scanning electron microscopes. A FEI Quanta 200 with a tungsten filament equipped with a Hikari EBSD detector was used for scans with step sizes of 2 μm to image the grain structure in the entire weld fusion zone. A Philips XL 30S with a field emission gun and a DigiView II EBSD detector were used for small step-size increments of 0.06 to 0.2 μm to zoom in on individual fusion zone grains. Both systems are equipped with EDAX TSL data collection software.

Vickers microhardness testing was performed on a calibrated Leco AMH43 microhardness testing system with load range from 9.8 to 4900 mN. The indentations were made using a 490 mN load, and were manually

measured using a 50 \times objective to determine the Vickers Hardness indentation diagonal lengths, which were typically about 20 μm corner to corner.

Nanoindentation hardness testing was done using a spherical indenter to measure load-depth curves that could be converted into approximate stress-strain material behavior. This method was particularly useful for estimating the stress-strain behavior of the welds, since the fusion zones were too small for a standard tensile test method. The 21-6-9 SS samples (polished, but not etched, base and weld metal) were tested using a G200 Nanoindenter from Keysight. A 50 μm radius spherical diamond tip was used during these tests. The advantages of this nanoindenter are that it has high load and displacement resolution, on the order of 50 nN and 1 nm, respectively, and with the high load option can go up to 10 N of force. Due to the relatively large diameter of the sphere coupled with the high strength of 21-6-9 SS, the high load option was used for these tests. In addition, this nanoindenter can apply an oscillating signal on top of the load signal which permits the stiffness of the material to be measured continuously (CSM) as a function of depth. All the tests were run using the high load and CSM options to measure the stiffness which is used in the calculation of stress and strain.

Since the samples were polished before indentation, features from the etched micrographs, such as the curved regions from the fusion zone, or the ledge from the step joint, are used to give an approximate delineation of the different zones. The nanoindenter can position indents within 1 micron of the specified location, and indentations were positioned well within each zone. The loading rate was 50 nm/second for each indent to a depth of 7000 nm, which corresponds to a strain rate of about 1×10^{-4} /second. These parameters were selected to match the strain rate of the standard tensile tests, and reach a strain of about 10 pct. In order to convert the load, displacement, and stiffness data from the indentation test to indentation stress and strain, calculations were performed using the procedure detailed elsewhere.^[4,9] The contact depth, h_c is calculated as follows:

$$h_c = h - 0.75 \frac{P}{S} \quad [1]$$

where h is the displacement, P is the load, and S is the contact stiffness, all of which are taken directly from the

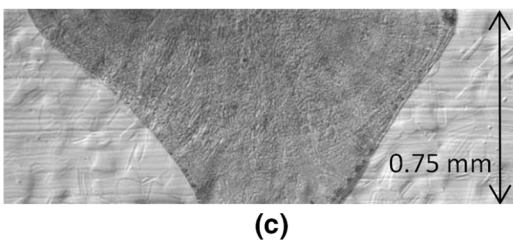
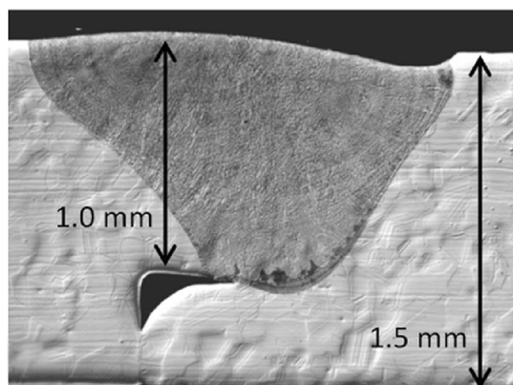
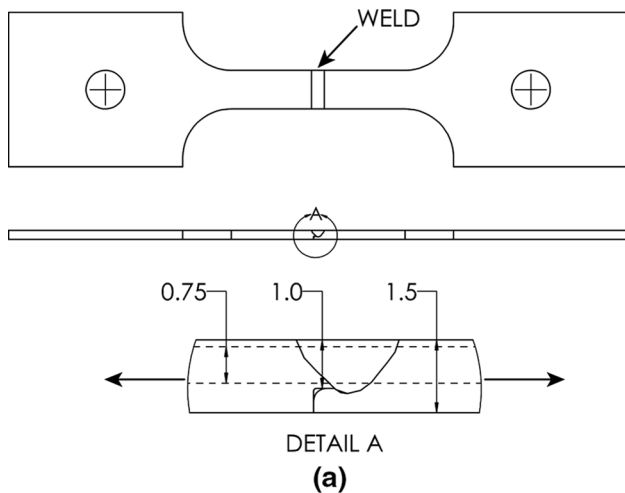


Fig. 2—(a) Illustration of the top and side views of cross-weld tensile bar with dimensions in mm. (b) Micrograph of the full-thickness as-welded coupon. (c) Cropped photo illustrating the cross section of the weld coupon after milling to remove the unwelded material below the step, the weld reinforcement, and the weld undercut (see dashed lines in detail A). The horizontal arrows indicate the tensile axis direction relative to the weld cross section.

nanoindenter. From the contact depth, the contact radius, a is

$$a = \sqrt{2h_c R_i - h_c^2} \quad [2]$$

where R_i is the radius of the indenter. The indentation strain, ε , is defined as follows:

$$\varepsilon = \frac{h_c}{2.4a} \quad [3]$$

And the indentation stress is as follows:

$$\sigma_{\text{ind}} = \frac{P}{\pi a^2} \quad [4]$$

To relate the indentation stress to the uniaxial stress, the Tabor relationship is used where

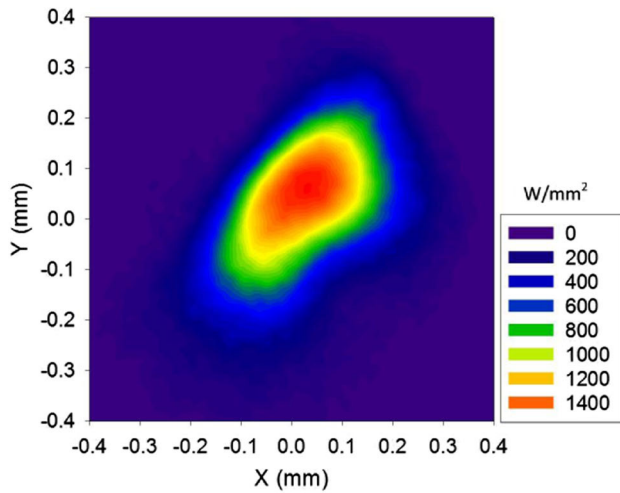
$$\sigma_{\text{uniaxial}} = \frac{\sigma_{\text{ind}}}{T} \quad [5]$$

where T is the Tabor factor that can be estimated by correlating the indentation load displacement curve with a known uniaxial stress-strain curve of the material.

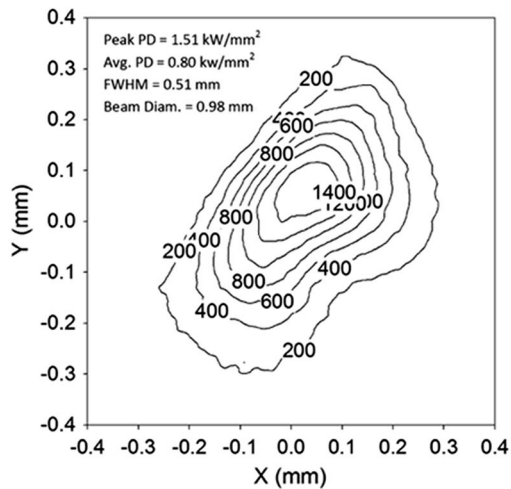
III. ELECTRON BEAM WELDS AND MICROSTRUCTURE

Electron beam welds were made using 110 kV, 5.5 mA (605 W) at a weld speed of 1524 mm/minute, with a +30 mA defocus above the surface. This beam was characterized with the Enhanced Modified Faraday Cup and shown to have a peak power density (PPD) of 1.5 to 1.6 kW/mm², a beam diameter ($1/e^2$) of 0.90 to 1.0 mm, and a beam full-width half-maximum (FWHM) of 0.50 to 0.55 mm. A representative power density distribution for this weld is shown in Figure 3. Note that the beam is not circular at this level of defocus, and has an elliptical shape with an aspect ratio of approximately 1.8:1. A typical cross section through the resulting weld is shown in Figure 2(a), and a summary of the EB welding parameters, weld depths, and weld widths is presented in Table II from cross sections taken from 6 welds. The weld penetrations varied from 0.98 to 1.14 mm, while the weld widths across the top surface varied from 1.51 to 1.56 mm. Undercutting appears on one side of the top surface that measures $52.7 \pm 5.4 \mu\text{m}$. The maximum undercut was measured to be $58 \mu\text{m}$, leaving at least 0.800 mm of full weld fusion zone above the step for the removal of the 0.750 mm thick milled tensile samples.

At high magnifications, the 21-6-9 SS weld microstructure was shown to be considerably different than the base metal microstructure. Figure 4(a) shows the base metal microstructure which consists of equiaxed grains that have an average grain diameter of approximately $50 \mu\text{m}$. Annealing twins are present in many of the grains, and small inclusions are randomly dispersed. Horizontal bands appearing in the base metal microstructure are believed to be due to the effects of chemical segregation during ingot casting and subsequent hot working and rolling, and are often observed in 21-6-9 SS plate. No delta ferrite was observed or measured in the base metal portions of the samples. The weld microstructure is shown at the fusion boundary in Figure 4(b) and in the central portion of the fusion zone in Figure 4(c). The majority of the microstructure consists of austenite (light etching phase) with some remnant delta ferrite (dark etching phase). The majority of the microstructure appears to have been formed by the solidification of primary ferrite with second-phase austenite (FA) mode where the primary ferrite dendrites that form during solidification partially



(a)

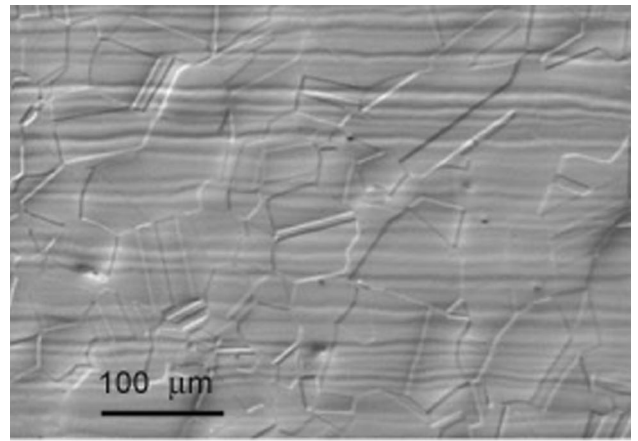


(b)

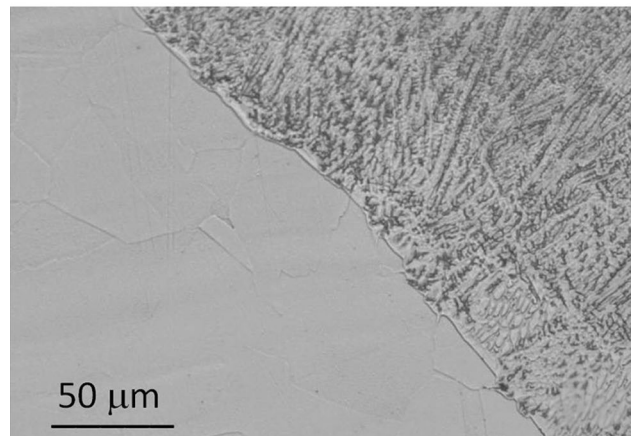
Fig. 3—Power density distribution for the electron beam, as measured by the EMFC diagnostic. (a) Pseudocolor plot and (b) contour plot and beam statistics.

transform to austenite during cooling.^[10] The remaining ferrite at room temperature has a vermicular/skeletal morphology, where the ferrite is concentrated at the original cores of the ferrite dendrites. This residual ferrite represents only a small fraction of the original primary ferrite phase that formed during solidification.

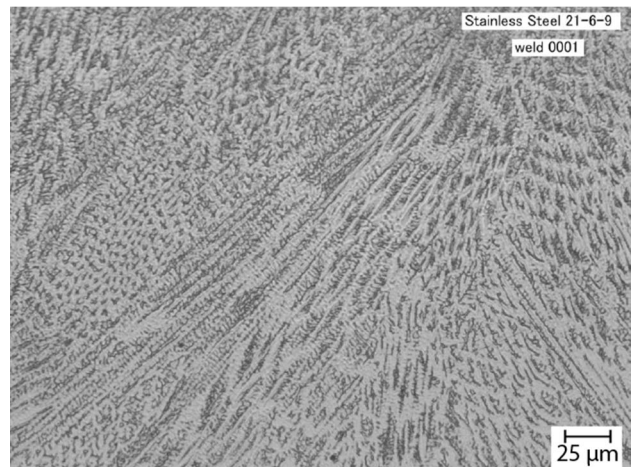
Figure 5(a) shows a higher magnification micrograph of the fusion boundary, where the remaining ferrite can be seen more clearly, and represents about 3 to 5 pct of the fusion zone microstructure in this location. Epitaxial regrowth of austenite from the base metal (1 to 2 μm) is followed by a zone ($\sim 10 \mu\text{m}$) that is difficult to interpret and is likely to have initiated as primary austenite (AF), which then transitions to the primary ferrite (FA) mode of solidification deeper into the fusion zone. Also note the grain boundary ferrite formed near the heat-affected zone at the upper left portion of the fusion zone. Figure 5(b) shows a higher magnification micrograph near the center of the fusion zone, which clearly solidified in the FA mode with skeletal ferrite present



(a)



(b)



(c)

Fig. 4—High-magnification photomicrographs of: (a) the base metal with a grain size of approximately $50 \mu\text{m}$, (b) the fusion boundary of weld, and (c) the central portion of the fusion zone showing the cellular/dendritic microstructure with a primary spacing of approximately $5 \mu\text{m}$.

throughout the majority of the microstructure, and lacy ferrite^[10] present in the upper right-hand side of the micrograph. The ferrite content appears to vary between

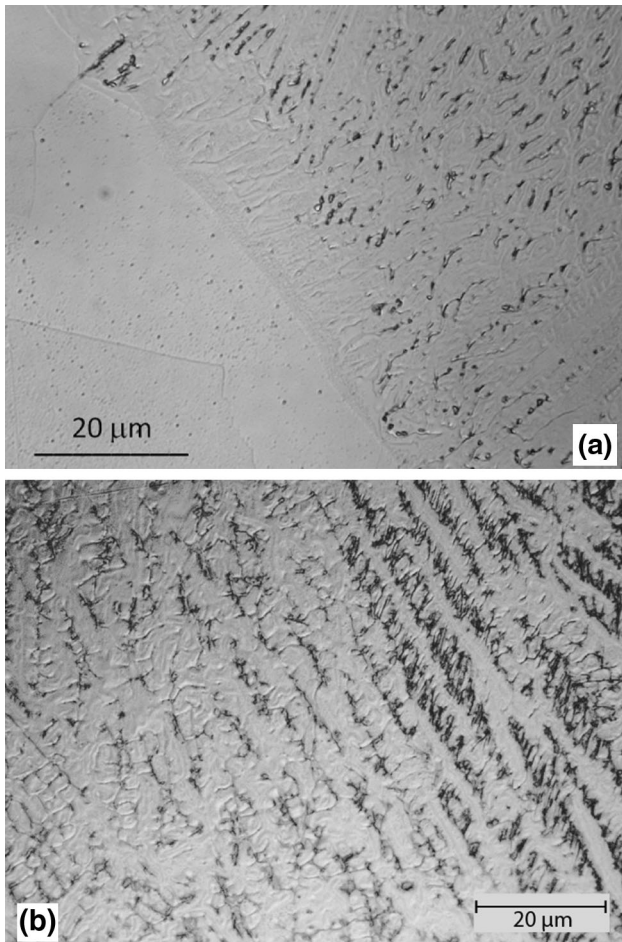


Fig. 5—High-magnification micrograph (a) the fusion line of the weld and (b) the center section of the fusion zone. The dark etching phase is residual delta ferrite. Both photos shot at $\times 1000$.

3 and 10 pct depending on the local ferrite morphology. The higher amount of ferrite observed in the microstructure relative to that measured by the Magne-Gage (~ 1 pct) is related to the inherent error of measuring ferrite with the Magne-Gage on small weld samples that incorporate base metal (0 pct ferrite) into the reading.

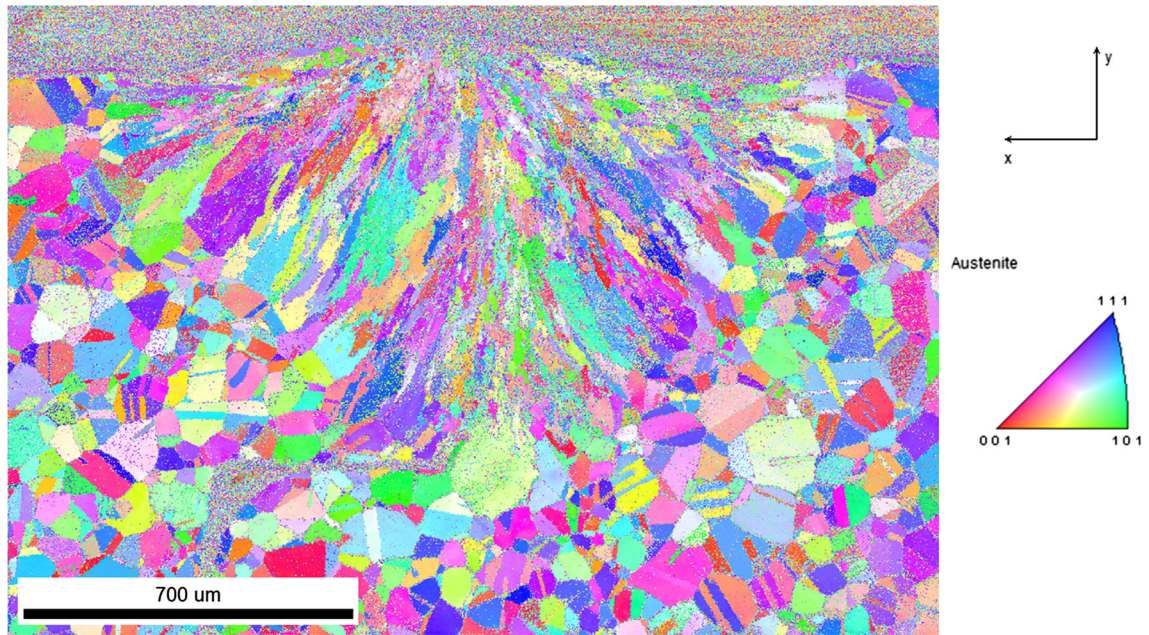
Figure 6(a) shows an orientation image map obtained from the complete cross section of one of the welds, including the base metal grains. The speckled top portion of the figure is from attempts to index points that are not part of the specimen; these data were removed from all further analysis as it is not part of the specimen. The EBSD measurements are made with an orientation perpendicular to the cross section, which is in the welding direction, and is shown using the inverse pole figure coloring scheme. The annealed base metal does not show preference for any particular crystallographic orientation and has apparent annealing twins in many of the grains. The weld has a columnar macrostructure with elongated grains forming in a pattern that follows the heat flow direction from the fusion zone boundary to the top center of the weld.

Again, no preference for any particular crystallographic orientation is seen in the weld. Pole figures plotting the orientation distribution of the base metal and the weld fusion zone are shown in Figures 6(b) and 6(c), respectively. It can be clearly seen that there is no preference for any particular crystallographic orientation in either the base metal or the weld, and the maximum intensity is low indicating non-textured microstructures. It is to be noted that since the pole figures are generated from a small number of grains they have a speckled appearance. In Figure 6, a large step size of $2 \mu\text{m}$ was used to map the entire weld, and at this resolution, the weld grains index as FCC austenite, indicating that the weld contains only a small amount of finely distributed BCC residual ferrite.

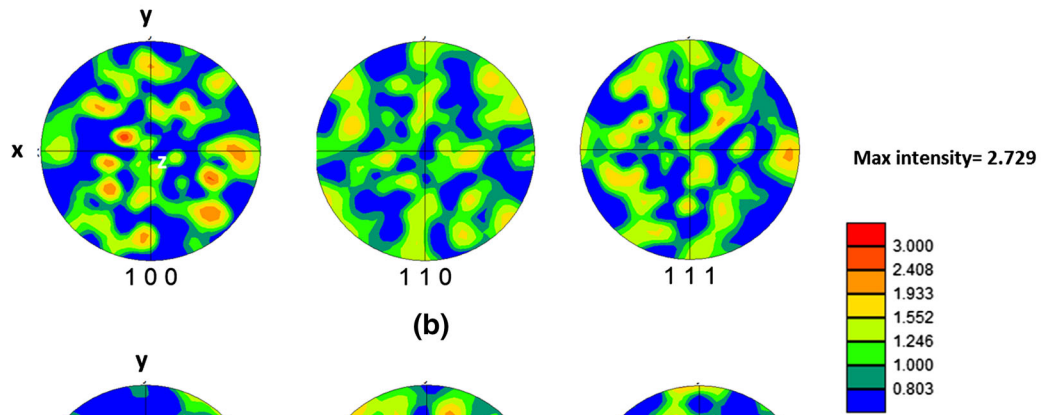
Figure 7 shows an orientation image map obtained from longitudinal section taken near the centerline of the weld. The weld travel direction is from left to right in this figure, where the fusion zone grains are angled normal to the trailing edge of the weld pool. This image was made using a large step size of $2 \mu\text{m}$ to include the full thickness of the sample and base metal grains below the fusion zone. The horizontal line represents the step of the weld joint that was not completely consumed by the weld at this location. The results show that the annealed base metal again does not show preference for any particular crystallographic orientation and has apparent twins in many of the grains. The weld fusion zone has a columnar macrostructure, dominated by austenite grains that are elongated along the heat flow direction from root to the top of the weld. Pole figures plotting the orientation distribution of both the base metal and the weld fusion zone grains are shown in Figures 7(b) and 7(c), respectively, can clearly indicate a non-textured microstructure. It is to be noted again that the pole figures are generated from a small number of grains, which gives them a speckled appearance.

The important information from the EBSD orientation maps shown in Figures 6 and 7 is that, although there is a columnar nature to the growth of the predominantly austenite phase in the weld fusion zone, the grain orientations are randomly distributed in both the cross section and longitudinal sections of the weld. The distribution of grain orientations is a consideration when modeling the mechanical behavior of welds.

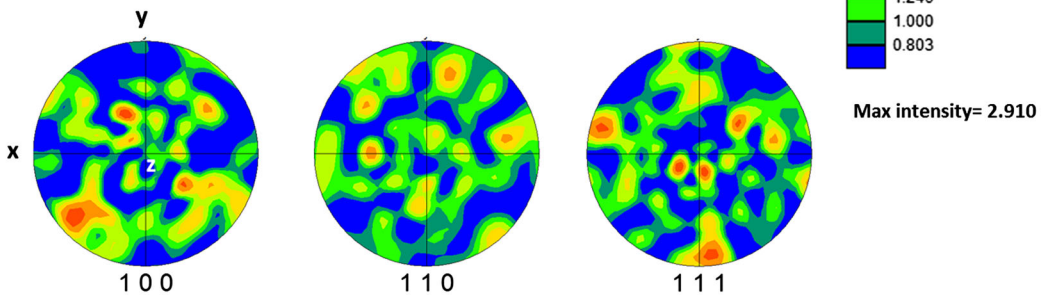
EBSD mapping was further carried out at finer step sizes ranging from 0.06 to $0.2 \mu\text{m}$ inside the fusion zone in an attempt to identify and quantify the residual ferrite content. Figure 8(a) shows the FCC, austenite, inverse pole figure map where black indicates a phase other than austenite. It is clear that austenite is the majority phase with the second phase showing up mainly inside the austenite grains. Some second phase also appears along the grain boundaries, but it is not clear if this is a different phase or overlapping EBSD patterns at the grain boundary. Figure 8(b) shows the BCC, ferrite, inverse pole figure map where black indicates a phase other than ferrite, which is austenite in this case. This figure is the inverse of Figure 8(a), since only BCC and



(a)



(b)



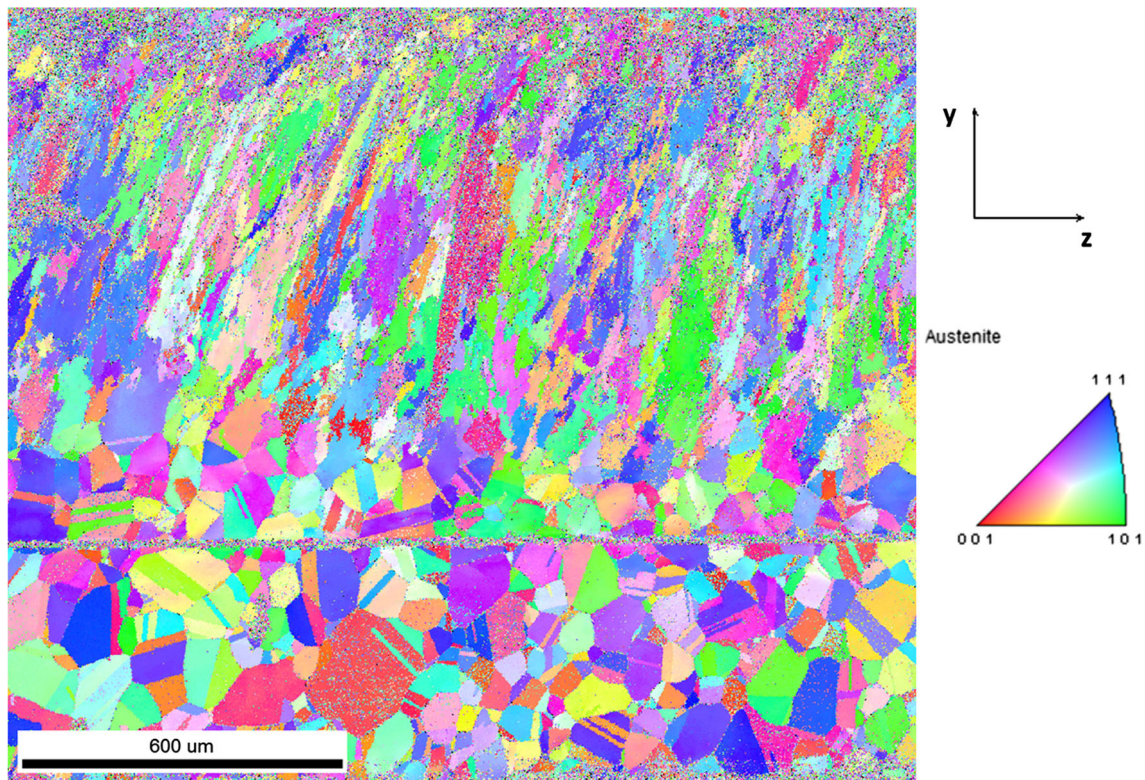
(c)

Fig. 6—(a) EBSD orientation image map obtained with a $2\ \mu\text{m}$ step size from the complete cross section of one of the welds, including the base metal grains, (b) pole figures showing random grain orientation in the base metal, and (c) pole figures showing random grain orientation in the weld fusion zone.

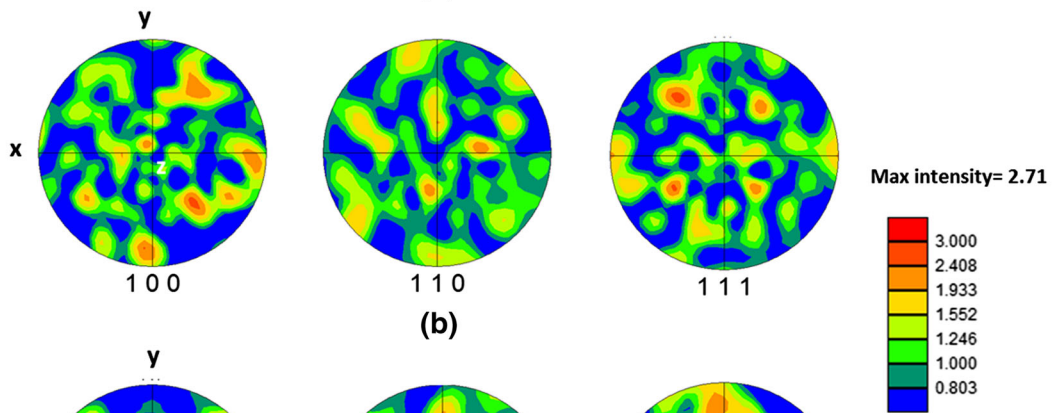
FCC phases are present in this weld. In this fine scale map, the residual ferrite is identified, but only in very small amounts since the residual ferrite dendrite cores are less than $1\ \mu\text{m}$ wide. Quantitative EBSD measurements of the amount of ferrite in the fusion zone at this location showed the ferrite content to be 4 pct, which is similar to the estimated amounts based on optical microscopy.

IV. MECHANICAL PROPERTIES OF THE BASE METAL AND WELDS

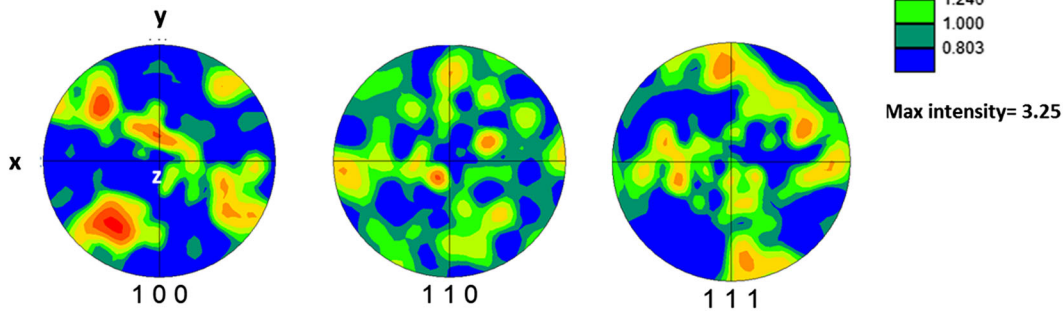
Table III summarizes the microhardness measurements that were made on the base metal, the electron beam fusion zone, and the HAZ for each of the 6 welded coupons. Here, we will refer to the HAZ as the region within $50\ \mu\text{m}$ of the fusion boundary, where



(a)



(b)



(c)

Fig. 7—(a) EBSD orientation image map obtained with a $2\ \mu\text{m}$ step size from the longitudinal section of one of the welds, including the base metal grains, (b) pole figures showing random grain orientation in the base metal, and (c) pole figures showing random grain orientation in the weld fusion zone.

microhardness readings were taken. A total of 36 hardness measurements were made on the base metal samples, showing that the base metal had an average hardness of 212.1 ± 10.9 HV. These values correspond

to annealed 21-6-9 SS sheet, which has a handbook value of RB 94 (HV 213).^[11] After welding, the fusion zone hardness was measured at 254.4 ± 9.7 HV based on 62 measurements made in the 6 welds. These results

show a 20 pct increase in hardness after welding relative to the 21-6-9 SS base metal, due to the fine two-phase weld solidification structure as described above. In the FZ, second-phase strengthening is provided by the presence of ferrite, in addition to a refined microstructure.

Additional microhardness measurements were made in the HAZ of the welds by placing the indenter in the

base metal at a distance of 1 to 2 indentation distances (20 to 40 μm) from the weld fusion line. The resulting measurements showed HAZ hardness values midway between the weld fusion zone and the base metal of 232.1 ± 13.9 HV. The apparent strengthening of the HAZ is most likely due to the indentation being affected by the nearby harder weld metal that impacts plastic flow during indentation, based on the belief that there should be no HAZ hardening mechanisms in the annealed 21-6-9 SS heat-affected zone. It is also possible that residual stresses in the HAZ are contributing to an increased hardness in this region.

A. Stress–Strain Behavior of Cross-Weld Tensile and Base Metal Samples

The base metal and two different types of cross-weld samples were tensile-tested to failure in both regular (101.6 mm long) and mini (25.4 mm long) configuration dog-bone shaped samples. Figure 9 shows the failure behavior for each of the six different tensile bar configurations. The base metal samples for the mini (a) and regular (d) tensile configurations failed approximately in the middle of the gage length with necking occurring mostly through the thickness of the bars. The welded samples that were milled to remove the effects of the unwelded step and weld reinforcement for the mini (b) and regular (e) tensile configurations failed approximately half-way between the weld and the radius that forms the tensile grips. In both cases a “lump” of weld metal is left behind where the stronger weld fusion zone deforms less than the base metal away from the weld. The final failures have a similar necking appearance to the base metal samples. The welded samples that were pulled in the full-thickness, as received, condition for the mini (c) and regular (f) tensile configurations failed in a completely different manner. Due to the reduced amount of load bearing material above the step, the samples failed in the base metal close to the weld, tearing through the base metal and HAZ with less apparent necking and less measured strain to failure than the other samples.

Figure 10 shows close-up photos of the necked regions of the broken mini tensile samples. The base metal sample is shown in (a) and (b) for the side and top views of the fractured sample, respectively. Thinning of the sample through the thickness and across the width of

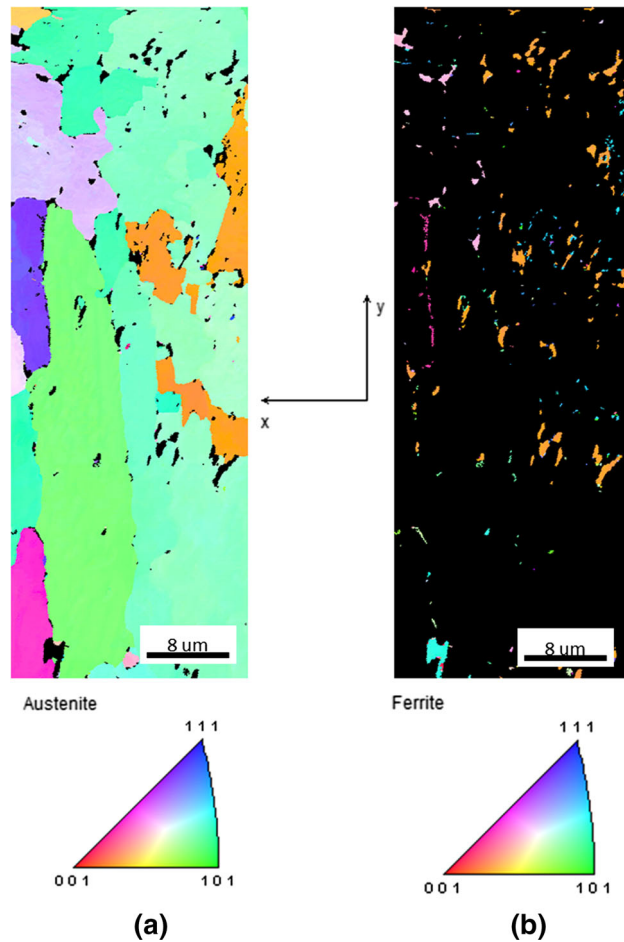


Fig. 8—EBSD orientation image map acquired on a fine scale from the fusion zone of the weld (a) FCC austenite inverse pole figure map where black indicates a phase other than austenite. (b) BCC ferrite inverse pole figure map where black indicates a phase other than ferrite.

Table III. Vickers Microhardness Measurements (490 mN Load) Made on the 21-6-9 Base Metal, Weld HAZ, and Weld Fusion Zone

Weld	Base Metal Hardness Avg/STD (HV)	HAZ Hardness Avg/STD (HV)	Weld Metal Hardness Avg/STD (HV)
1	215.8/11.2	226.8/10.4	258.9/10.0
2	212.5/6.50	241.1/14.3	257.8/9.60
3	216.0/6.60	225.8/8.30	249.6/10.1
4	209.5/10.0	226.7/10.1	258.2/10.9
5	201.0/7.70	235.5/18.0	247.2/13.2
6	218.3/7.50	237.4/12.1	254.9/6.60
Avg./STD	212.1/10.9	232.1/13.9	254.4/9.7
Number of Points	36	49	62

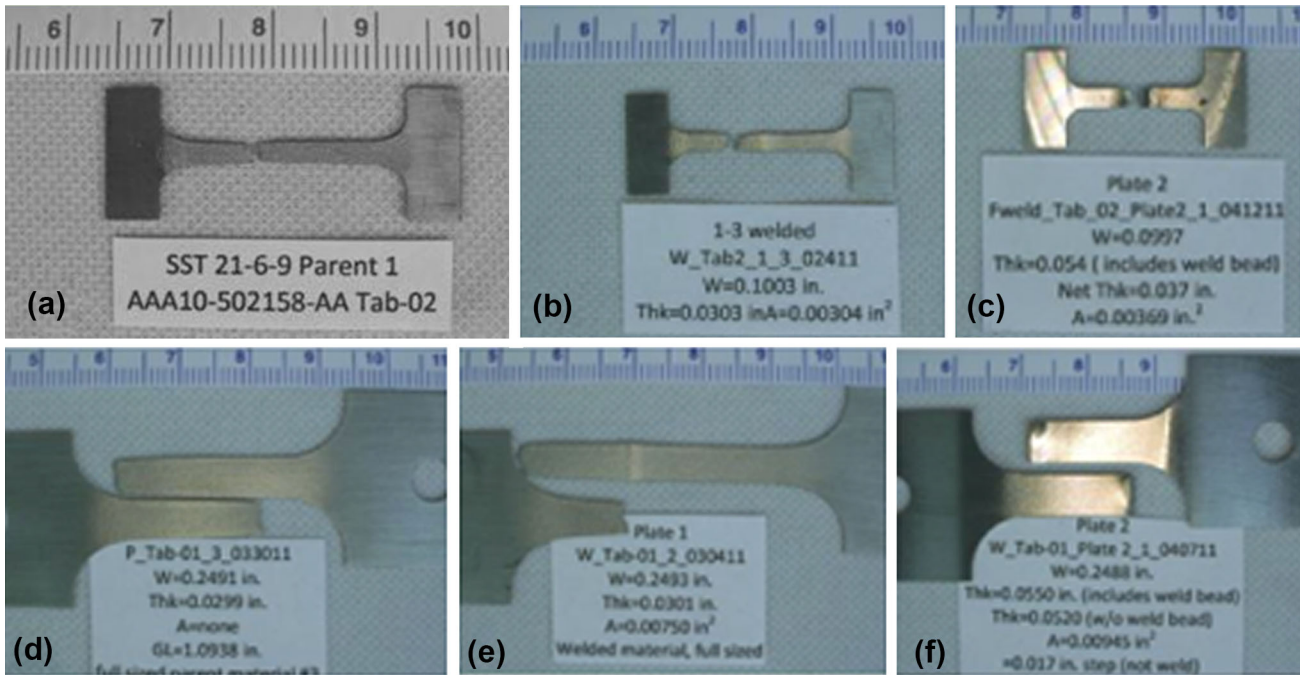


Fig. 9—Photographs of representative tensile bars for each of the six different configurations. (a) and (d) show base metal samples, (b) and (e) show milled weld samples, while (c) and (f) show as-welded samples after tensile testing. The small divisions in the scale markers in the photographs are 1 mm increments.

the sample is apparent. The failure is ductile in appearance, and final failure occurred with the formation of a shear lip at approximately 45 degrees to the tensile axis. The milled cross-welded sample is shown in (c) and (d) for the side and top views of the fractured sample, respectively. The weld location is marked in the figures and it is clear that the fracture occurred well away from the weld. It can also be seen that the weld region deformed less than the base metal, being wider and thicker than the adjacent base metal. Just like the base metal sample, the failure is in the base metal and the final failure occurred with the formation of a shear lip at approximately 45 degrees to the tensile axis. The full-thickness, as-welded, cross-weld sample is shown in (e) and (f) for the side and top views of the fractured sample, respectively. The side views show that the location of the failure is adjacent to the fusion line of the weld in the reduced thickness portion of the sample. As before, the final failure is ductile in appearance, forming a 45 degrees shear lip relative to the tensile axis. Some localized deformation extends from the base of the weld and appears to follow a columnar weld grain boundary into the weld fusion zone. The top view of the failed sample shows narrowing occurring on the side of the weld with the reduced section thickness, and little to no narrowing on the thick section side of the weld.

This same as-welded tensile sample was then polished and etched in cross section to show the deformation and failure locations more clearly. Figure 11(a) shows the sample lightly polished and etched, indicating that the weld region above the step is deforming, while the remainder of the weld appears comparatively unstrained. Figure 11(b) shows the same sample after lapping more deeply below the surface and then

repolishing and etching, showing that the final failure occurred in the base metal adjacent to the fusion zone. A high-magnification photo of the failed region adjacent to the fusion line is shown in Figure 11(c). The individual base metal grains near the fusion line contain wavy deformation bands. These bands are likely the result of strain-induced martensite, which forms during deformation and is known to be the principal strain hardening mechanism in stainless steels^[12] and is also known to form in 21-6-9 SS at high strain rates.^[13] Microhardness measurements made in necked region of the failed sample showed that the hardness is 394.8 ± 12.0 HV for 9 data points, which is considerably harder than the undeformed base metal (212.2 HV) or the weld (254.4 HV).

Figure 12 plots the uniaxial engineering stress versus engineering strain tensile behavior of the base metal samples for both the mini and regular tensile configurations, and the resulting data are summarized in Table IV. The base metal tensile samples showed yield stresses (σ_y) that varied from 345 to 365 MPa, with the mini tensile bars having yield strengths on the lower end of this range. All curves show significant strain hardening with ultimate tensile strengths (UTS) varying between 701 to 720 MPa, with the mini tensile bars on the upper end of this range. The elongations at failure varied from 47 to 62 pct for the base metal samples using the laser extensometer with the 25.4 mm gage length. The mini samples, with the smaller 5.715 mm gage length, showed high elongations, up to 80 pct. Note that the extensometer was removed prior to failure of the mini samples, resulting in the small load drop observed in the plotted curves. The subsequent stress-strain behavior after the extensometer was removed was

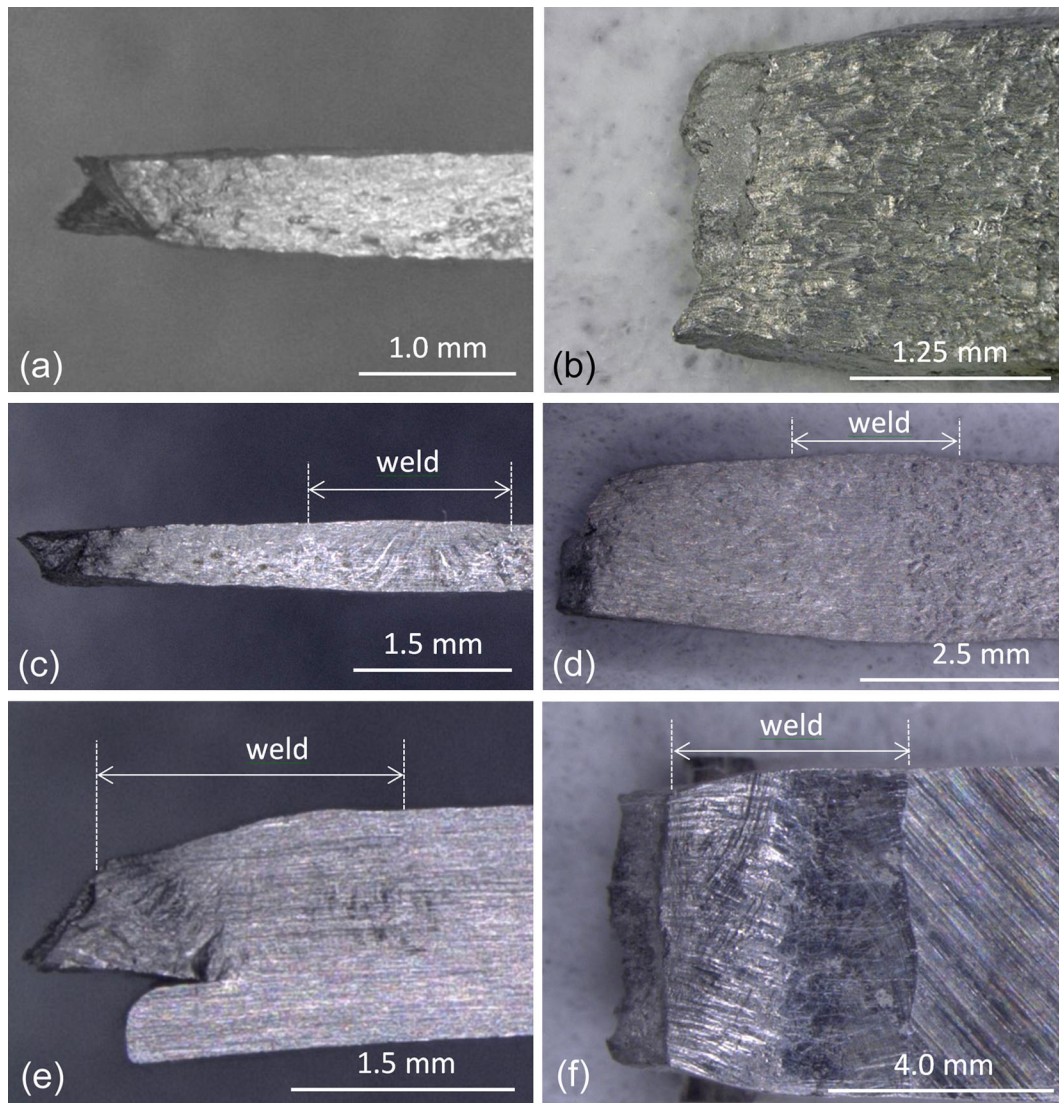


Fig. 10—Close-up photos of the necked regions of the mini tensile test bars: (a) and (b) side and top views of the base metal sample, respectively; (c) and (d) side and top views of the milled cross-weld sample, respectively; (e) and (f) side and top views of the full-thickness cross-weld sample, respectively. Various magnifications horizontal arrows indicate location of the welds.

estimated from the load versus crosshead displacement measurements, which is an approximation that does not match the strain hardening rate measured by the extensometer.

Figure 13 plots the engineering stress versus engineering strain curves for the milled weld samples. These samples behaved nearly identically to the base metal samples with yield strengths varying from 364 to 384 MPa, and ultimate strengths varying from 716 to 730 MPa as summarized in Table IV. The elongations to failure for the regular sized samples were similar to those of the base metal, varying from 54 to 63 pct, while those for the mini samples again displayed slightly higher elongations at failure. Observations of the tensile samples showed that in all cases, the milled cross-weld tensile samples failed in the base metal due to the higher strength of the weld. Because of this, the yield and ultimate strengths measured on these samples essentially match those of the base metal samples, showing that this

sample configuration is not good for measuring the true weld fusion zone properties.

Figure 14(a) plots the engineering stress versus engineering strain results of the full-thickness, as-welded, samples. In this configuration, the weld reinforcement and unwelded portion of the step were not removed, as illustrated in Figure 14(b). The tensile behavior is quite different than the milled cross-weld tensile samples. Yield strengths, based on the area of the sample above the weld step, were considerably higher than the other samples with values up to 526 MPa for the standard samples, and values up to 521 MPa for the mini samples. These strengths are 25 to 43 pct higher than in the other two sample configurations. The difference in behavior can be explained with the aid of Figure 14(b) that schematically illustrates the full-thickness test sample. In these as-welded samples, there is a region of reduced area, and thus high stress concentration, directly above the unwelded step, which contains a large fraction of

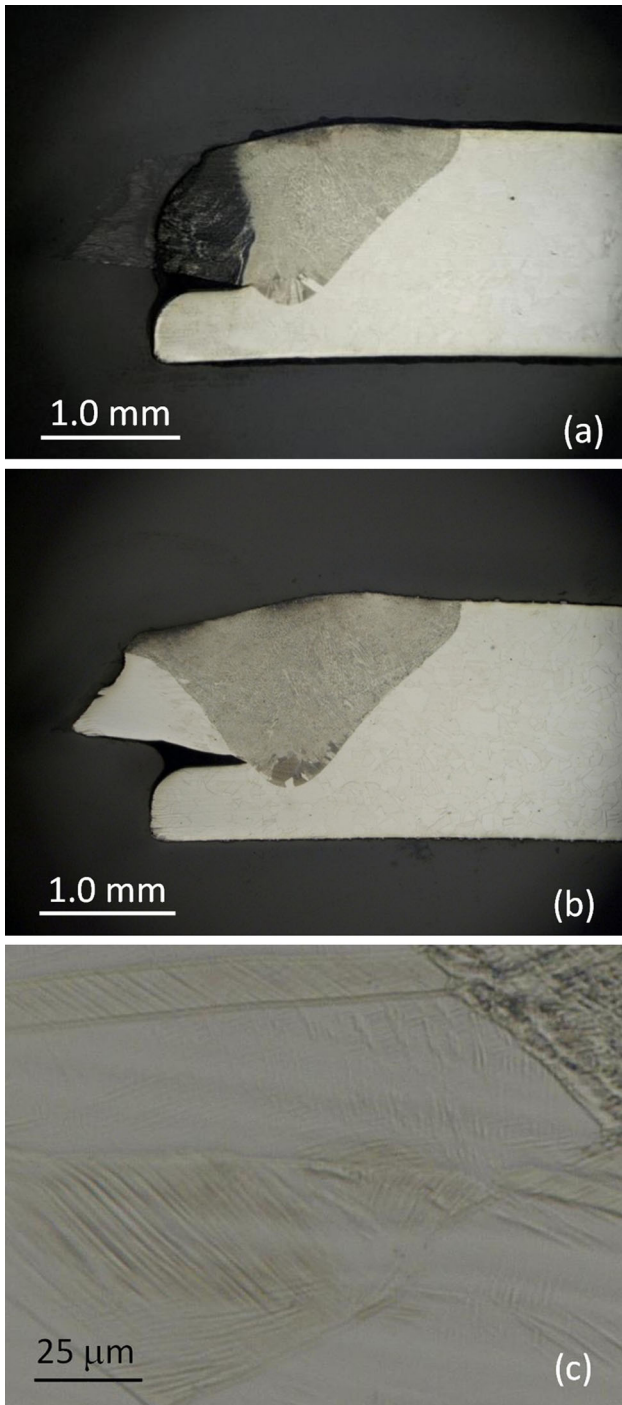


Fig. 11—Full-thickness mini sample after tensile testing. (a) After light polish of surface, showing deformation in the region directly above the unwelded portion of the step. (b) After lapping the sample to a depth ~1 mm below the surface to show necking and final failure location in the base metal. (c) High-magnification micrograph of the fusion line in the failed portion of the sample, showing deformation bands in the base metal.

welded metal. The higher yield strengths measured on the full-thickness samples are partly based on the fact that the high strain region contains some fraction of higher strength welded metal. In addition, the presence of the step joint can cause bending stresses to develop in

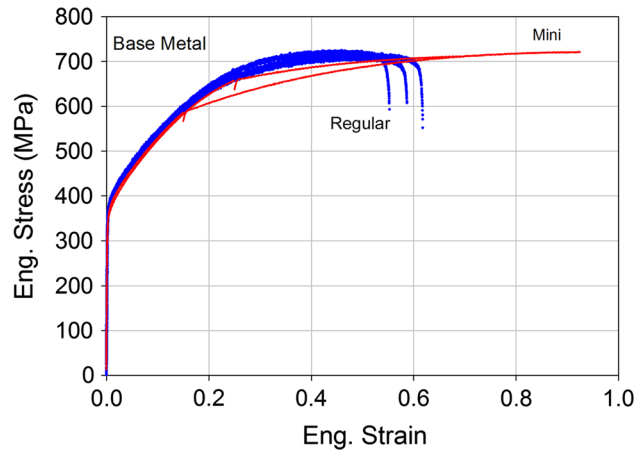


Fig. 12—Base metal stress-strain curves for the regular and mini tensile bars.

the localized strain region above the step and may also contribute to the an increased yield strength in those samples. The elongations were also different than the milled cross-weld samples. The regular-sized full-thickness cross-weld samples all failed with total elongations of only 10 pct, whereas the mini samples failed between 22 and 27 pct elongation. The reduced elongations are also likely to be the direct result of the strain localization above the weld step and the fact that the extensometers span a much wider area than the highly strained region. Peak loads were used to calculate the UTS based on the reduced cross-sectional area of the sample above the unwelded portion of the step, showing values between 705 to 760 MPa, which are similar to the tensile tests in the other sample geometries. Although the stress state in these samples is more complex than the other uniaxial testing configurations, the geometry localizes the stain to the weld region and permits an approximate measurement of properties of the weld material, which is shown to be stronger and less ductile than the base metal. Note also, that the measured modulus data for the full-thickness samples were not accurate due to the change in section thickness and bending of the samples. This effect is magnified with the shorter gage length mini sample where a larger fraction of necking is present in the gage length.

In summary, the tensile test results show that the cross-weld samples failed in the base metal portions of the tensile bar and produced strengths comparable to the base metal samples having a 0.2 pct offset yield strength of 366 ± 16 MPa, an ultimate strength of 726 ± 15 MPa, and a Young's modulus of 202.7 ± 6.6 GPa. The engineering strain at failure measured on the regular sized samples with a 25.4 mm gage length was approximately 60 pct, while the mini samples for both the base metal and the milled cross-weld configurations had higher measured elongations due to the larger fraction of necked region in the 5.715 mm gage length. The full-thickness cross-weld tensile samples are representative of the real weld and show highly localized strain behavior in the thinner portion of the step welded joint. The associated change in thickness near the

Table IV. Summary of the Tensile Test Results on the Base Metal, Milled Cross-Weld Tensile Samples, and Full-Thickness Tensile Samples

Sample Condition	Width (mm)	Thickness (mm)	Area (mm ²)	Gage Length (mm)	Xhd Speed (mm/min)	Young's Modulus (GPa)	Elon. (Pct)	Yield Strength (MPa)	Ultimate Strength (MPa)
Base Metal									
Mini	2.56	0.77	2.00	5.72	0.51	200	71	345	711
Mini	2.57	0.76	1.94	5.72	0.51	197	80	346	720
Regular	6.33	0.77	4.90	27.20	1.27	212	62	365	717
Regular	6.33	0.76	4.84	27.76	1.27	212	58	359	713
Regular	6.33	0.74	4.65	27.79	1.27	204	47	364	701
As-welded									
Mini	2.54	0.98	2.45	3.54	0.51	N/A*	24	462	705
Mini	2.54	0.90	2.26	3.51	0.51	N/A*	27	483	760
Mini	2.54	0.95	2.39	2.72	0.51	N/A*	22	521	747
Regular	6.32	0.97	6.13	27.46	1.27	N/A*	9.6	524	745
Regular	6.33	0.91	5.74	27.15	1.27	N/A*	9.5	526	739
Regular	6.30	0.94	5.94	27.02	1.27	N/A*	9.4	523	740
Welded/Milled									
Mini	2.56	0.76	1.94	5.72	0.51	193	73	384	727
Mini	2.56	0.78	2.00	5.72	0.51	197	69	383	729
Mini	2.55	0.77	1.94	5.72	0.51	204	73	375	725
Regular	6.33	0.78	4.90	27.52	1.27	197	63	369	720
Regular	6.33	0.77	4.84	27.72	1.27	197	54	364	716
Regular	6.33	.77	4.84	27.67	1.27	204	55	372	725

All samples tested at room temperature.

*Young's modulus not accurate due to sample bending in the as-welded cross tensile samples.

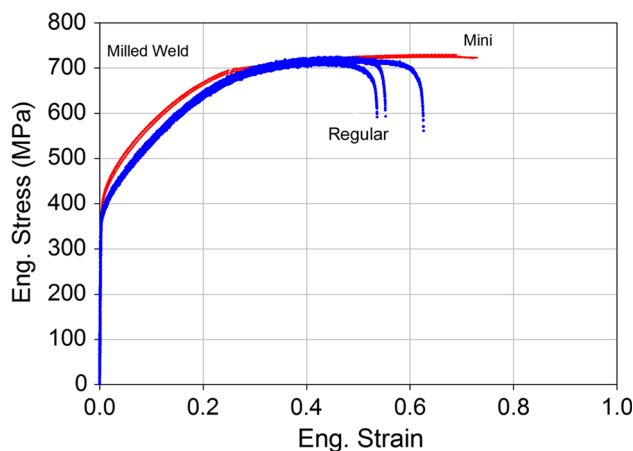


Fig. 13—Milled cross-weld sample stress–strain curves for the regular and mini tensile bars.

cross-tensile weld resulted in a reduced engineering strain at failure, higher yield strengths (506 ± 27 MPa), but similar UTS measurements as the other tensile test samples and configurations. Based on these results, other methods are required to determine the mechanical properties of the weld FZ since none of the cross-weld sample configurations produced representative weld FZ properties.

B. Nanoindentation Estimation of the Stress–Strain Behavior of the Welds

Uniaxial tension or compression testing is the standard method to obtain stress versus strain data.

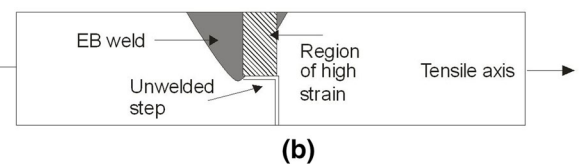
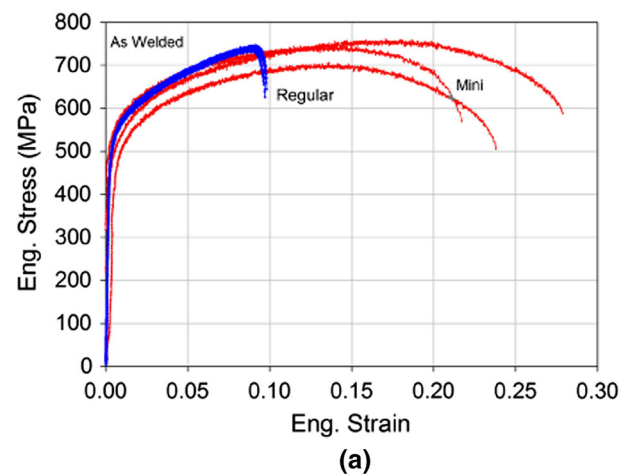


Fig. 14—(a) Full-thickness, as-welded, cross-weld sample stress–strain curves for the regular and mini tensile bars. (b) Schematic drawing of the as-welded sample illustrating the high strain region directly above the unwelded portion of the step.

However, there are times when the specimen or feature size is approaching dimensions that make it difficult to perform standard tests, as is the case for the small electron beam welds studied here. An alternate method that can be used to measure the stress–strain behavior of

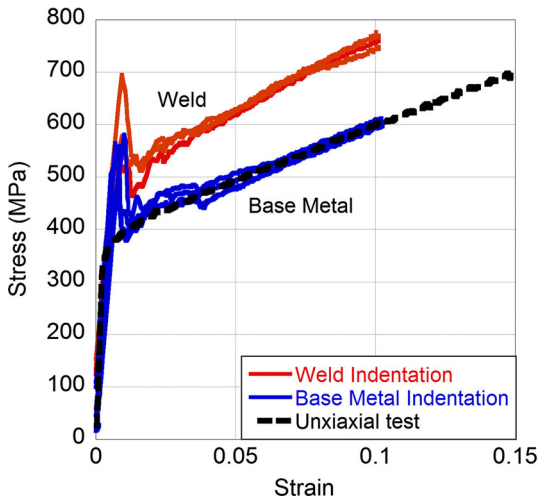


Fig. 15—Stress–strain data from the 21-6-9 SS base metal and the weld. The stress–strain data from the based metal indentation tests are compared to the uniaxial tests, as well as the weld indentation tests. A Tabor factor of 3.6 is applied to all of the indentation test data.

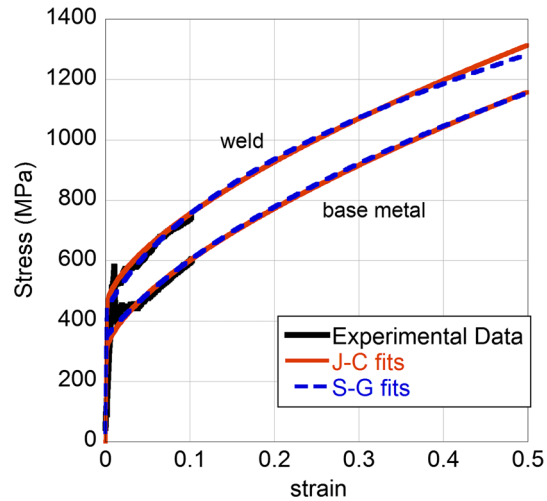


Fig. 17—Steinberg–Guinan (S–G) and Johnson–Cook (J–C) stress–strain curve fits for the 21-6-9 SS base metal and weld metal using MIDAS to extrapolate the material behavior to larger strains. Both fits are superimposed over the spherical indentation experimental data.

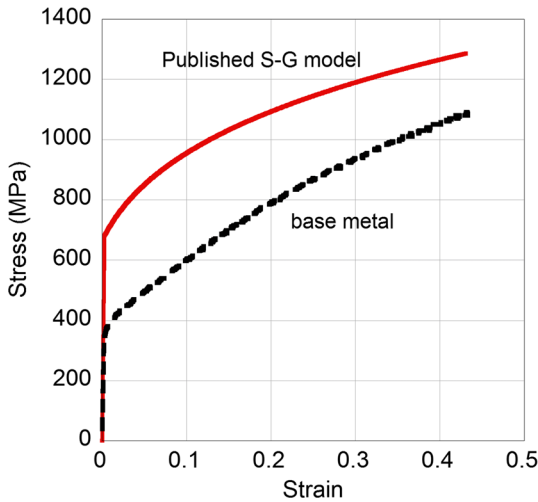


Fig. 16—Comparison of the published Steinberg–Guinan parameters (optimized for high strain rates) to the experimental data of this study for annealed 21-6-9 SS base metal measured at quasi-static strain rates.

small welds relies on an indentation technique. During indentation, the hardness of a material, defined as the load/area, is measured. The stress state during indentation however is much more complicated than in a uniaxial test and can be influenced by the shape and material of the indenter.^[3,4] During spherical indentation, the plastic zone develops gradually, allowing for the elastic-plastic transition to be probed in order to produce an indentation stress–strain curve. The spherical indentation method is used here to estimate the stress–strain behavior of the welded region of a 21-6-9 SS part, using the base metal, with known tensile behavior, for calibration.

Indentation tests were performed on the base metal and then compared with the uniaxial tension tests. The

data from the spherical indentation tests were converted to indentation stress and indentation strain using the method described in the procedure section. The correlation factor (Tabor relationship), to relate the indentation stress to the equivalent uniaxial stress, was then determined by matching to the uniaxial tests. This correlation factor was then used in calculating the corresponding stress–strain data for the weld sample. The main assumption is that the correlation factor is the same between the base metal and the welded 21-6-9 SS. In addition, estimates of the elastic modulus were determined from the CSM readings, showing that the base metal had a modulus of elasticity of 198.2 ± 1.6 GPa (six samples), and the weld had a modulus of elasticity of 190.1 ± 1.2 GPa (four samples). The nanoindentation results for the base metal compare well with the modulus values measured here in uniaxial tension with a base metal value of 202.7 ± 6.6 GPa (12 samples). The modulus of the weld measured by nanoindentation is approximately 4 pct lower than that of the base metal as measured by nanoindentation; the reason for the lower measured weld modulus is unclear at this point and will require additional analysis to determine the source of the discrepancy.

Representative indenter-based stress–strain curves for the base metal are shown in Figure 15. In order to match the data, a Tabor factor of 3.6 was applied. The spherical indentation data show an initial overshoot in the stress before it matches the uniaxial data. The overshoot is most likely due to a combination of errors associated with the initial area function of the tip as it comes into contact with the surface^[4] and a lower dislocation density in the initial small volume probed by the nanoindenter. Local regions of lower dislocation density require a higher stress before a sufficient number of dislocations are generated to accommodate the imposed strain. Using the described analysis and Tabor factor, indentation stress–strain data for the welded

region, as well as a comparison between the base metal and weld region are also shown in Figure 15. The yield stress for the weld region is clearly higher as a result of its refined and two-phase microstructure. The strain hardening rate, however, is similar between the two types of materials, which suggests that the scale for the hardening mechanisms, such as dislocation interactions, is smaller than the grain size in the weld region.

The Vickers hardness data can be compared to the indentation stress–strain data by first converting the HV value to GPa [$\text{GPa} = 9.8 \times \text{HV}/1000$] and then dividing by the Tabor factor. Since the Vickers indenter is self-similar, meaning the plastic strain is constant as a function of depth, the Vickers hardness value corresponds to a plastic strain of around 8 pct. Using this methodology, the Vickers data correspond to a flow stress at 8 pct strain of 590 MPa for the base metal and 700 MPa for the weld region. These values are in good agreement with the indentation stress–strain data that show a stress of 560 and 700 MPa at 8 pct strain for the base metal and weld region, respectively.

To extrapolate the indentation data to larger strains, the Steinberg–Guinan model^[5] was used to fit the indentation data. The Steinberg–Guinan relationship has a similar form to the well-known Holloman equation and is defined as follows:

$$Y = Y_0 [1 + \beta(\varepsilon + \varepsilon_i)]^n \frac{G(P, T)}{G_0} \leq Y_{\max} \quad [6]$$

where Y_0 is the yield stress, β is the hardening coefficient, n is the hardening exponent, G_0 is the reference shear modulus, $G(P, T)$ is temperature- and pressure-dependent shear modulus, and Y_{\max} is the saturation stress representing the upper limit for the flow stress. For the experiments performed in this study, the ratio of the shear moduli was assumed to be 1.

As a point of reference, there are published parameters for the Steinberg–Guinan model for 21-6-9 SS.^[5,14] Since the published values are optimized for higher strain rates and Steinberg–Guinan is a rate-independent model, it is expected that the published 21-6-9 SS parameters^[5,14] would over-predict the strength in comparison to the quasi-static experimental data. Figure 16 shows the over prediction of the stress–strain behavior for the published Steinberg–Guinan data when compared to one of the experimental uniaxial stress–strain curves for the base metal from this study. Clearly, the Steinberg–Guinan published data need to be reevaluated for quasi-static strain rates. This was done by both fitting the base metal uniaxial stress–strain curves and

the nanoindentation results using the MIDAS framework.^[15] Fits were made out to 0.5 strain and are shown in Figure 17. The same approach was used to fit and extrapolate the nanoindentation results for the electron beam-welded material, and these results are also plotted in Figure 17 and show the increase in strength of the electron beam welds relative to the annealed 21-6-9 SS base metal. The Steinberg–Guinan model parameters for the base metal and weld are summarized and are compared to the published value^[14] for 21-6-9 SS given in Table V. Instead of having to create two separate set of parameters for both quasi-static and dynamic conditions, a strength model, which includes strain rate dependence, such as the commonly used the Johnson–Cook strength relationship can be used.^[6] While also empirically based, the Johnson–Cook model has parameters which account for the dependence on the strain rate and temperature, and has the following form:

$$Y = (A + B\varepsilon^n) \left(1 + C \ln \frac{\dot{\varepsilon}}{\dot{\varepsilon}_0} \right) (1 - T^{*m}) + C_p p \quad [7]$$

and

$$T^* = \frac{T - T_{\text{room}}}{T_{\text{melt}} - T_{\text{room}}} \quad [8]$$

where A is the effective yield stress at the reference strain rate, $\dot{\varepsilon}_0$ (1/s) and temperature, T_{room} (298 K [21.8 °C]), B is a strain hardening coefficient, n is the hardening exponent, C is the coefficient for the strain rate term, m is the exponential for the temperature dependence, C_p is the pressure coefficient, and p is the actual pressure. The results of the Johnson–Cook model are compared to Steinberg–Guinan in Figure 17, showing that both approaches can be used to represent the quasi-static uniaxial stress–strain behavior of 21-6-9 SS base metal and EB welds. The strain rate and temperature-dependent Johnson–Cook parameters were chosen to align with higher strain rate data on similar 21-6-9 SS base metal material.^[16] It is also assumed that weld material would have a similar strain rate and temperature dependence as the base metal. The fitting parameters for Steinberg–Guinan and Johnson–Cook are summarized in Tables V and VI, respectively.

V. SUMMARY AND CONCLUSIONS

Electron beam welding of annealed 21-6-9 stainless steel showed a significant hardening effect where the weld FZ is statistically harder than the annealed base metal. Metallographic characterization indicated that

Table V. Recommended Steinberg–Guinan Parameters for the 21-6-9 SS Experimental Weld Metal and Annealed Base Metal Values Under Quasi-Static Strain Rate Conditions, Compared to the Published Base Metal Value at High Strain Rates

Steinberg–Guinan Parameter	Definition	Base Metal Published Value ^[14] (high rate)	Base Metal Experimental Value (Quasi-Static)	Weld Metal Value (Quasi-Static)
Y_0	yield stress	0.0068 Mbar (680 MPa)	0.0035 Mbar (350 MPa)	0.0044 Mbar (440 MPa)
β	hardening coefficient	35	20	33
n	hardening exponent	0.23	0.5	0.375
Y_{\max}	saturation stress	0.025 (2.5 GPa)	0.025 (2.5 GPa)	0.025 (2.5 GPa)

Table VI. Recommended Johnson–Cook Strength Parameters for the 21-6-9 SS Weld Metal and Annealed Base Metal, Under Quasi-Static Strain Rate Conditions

Johnson–Cook Parameter	Definition	Base Metal Value (Quasi-Static)	Weld Metal Value (Quasi-Static)
A	effective yield stress at $\dot{\epsilon}_0 = 1/s$ and $T = RT$	450 MPa	680 MPa
B	hardening coefficient	2000 MPa	2000 MPa
n	hardening exponent	0.65	0.65
C	strain rate coefficient	0.032	0.032
m	temperature exponent	0.5	0.5
T_{melt}	melting temperature	2380 K (2106.8 °C)	2380 K (2106.8 °C)
T_{room}	ambient room temperature	295 K (21.8 °C)	295 K (21.8 °C)
$\dot{\epsilon}_0$	reference strain rate	1/s	1/s

the weld consists of a two-phase microstructure containing austenite plus residual delta ferrite. The primary mode of solidification was identified as ferrite with secondary austenite, followed by solid state transformation of the majority of the ferrite to austenite during cooling. The resulting microstructure is skeletal ferrite with some lacy ferrite observed near the center of the weld. The higher hardness of the weld is due to the observed fine two-phase solidification microstructure relative to the equiaxed large-grained austenitic base metal. Mechanical properties of the welds were further investigated using cross-weld tensile bars of different sizes and configurations and nanoindentation methods with a spherical indenter. From the results of these tests, the following conclusions were made:

1. The 21-6-9 weld solidifies mainly in the primary ferrite mode (FA), followed by transformation of a majority of the ferrite to austenite. The resulting weld microstructure varies from about 3 to 10 pct residual ferrite depending on the local ferrite morphology, as opposed to 0 pct ferrite in the annealed base metal. EBSD results confirm the majority phase as austenite, with a random grain orientation in the weld longitudinal and cross sections, even though the weld fusion zone has a strong columnar nature, with elongated grains following the heat flow direction.
2. Cross-weld tensile samples were not effective at measuring the mechanical behavior of the 21-6-9 stainless steel FZ metal since all failures occurred in the base metal regardless of tensile bar size or configuration. Results from the milled samples showed that the 0.2 pct offset yield stress (366 ± 13 MPa), ultimate stress (726 ± 15 MPa), and Young's modulus (202.7 ± 6.6 GPa) were largely independent of sample size and are similar to the properties of the base metal samples. Elongations at failure varied from 47 to 62 pct in the regular-sized milled samples with a 25.4 mm gage length, also similar to the base metal values.
3. The full-thickness, as-welded, cross-weld tensile samples did not match the results from the milled cross-weld samples or the base metal. The full-thickness samples showed higher yield strengths than the milled samples of 506 ± 27 MPa due to incorporation of stronger weld metal into the necked region near the final failure and strain localization in this sample above the step in the weld. Other factors, such as the presence of extra weld material above the weld surface and sample bending, complicate the tensile behavior of the as-welded samples. The measured elongations at failure were highly reduced in the as-welded samples as compared to the other sample configurations with a measured elongation at failure of only 10 pct in the regular-sized samples and 25 pct in the mini-sized sample.
4. Microhardness measurements confirm weld strengthening in 21-6-9 SS. The weld metal was shown to have a statistically higher Vickers hardness HV of 254.4 ± 9.7 , compared to the base metal hardness of 212.1 ± 10.9 .
5. Nanoindentation using a spherical indenter was used to generate a stress–strain curve to about 10 pct strain for the 21-6-9 EB weld metal, as calibrated by the base metal tensile tests. A Tabor factor of 3.6 was determined to produce the best fit of the 21-6-9 SS base metal indentation curve to the uniaxial tensile test data. Results showed that the weld metal has a yield stress of 440 MPa, which is approximately 26 pct higher than that of the base metal 350 MPa.
6. Uniaxial stress–strain models were fit to the quasi-static experimental data in order to extend the nanoindentation weld results to higher strains. The Steinberg–Guinan and Johnson–Cook parameters for each model were determined for both the weld and base metals under quasi-static loading conditions as summarized in Tables V and VI. It is notable that the published Steinberg–Guinan data for 21-6-9 SS produces yield strengths significantly higher than what is measured in uniaxial tensile experimental data at quasi-static strain rates. This difference is related to the fact that the Steinberg–Guinan published data are optimized for high strain rates.^[14]
7. The relative strength of the weld to the base metal is an important consideration for design when welded joints are present in the component. The results of the Steinberg–Guinan fit to the nanoindentation data under quasi-static strain rates indicate that the flow stress of the weld at 8 pct strain is $1.17 \times (696/592$ MPa) higher than that of the base metal.

ACKNOWLEDGMENTS

The authors would like to thank other LLNL employees who assisted with this work: Gilbert Gallegos for supplying the 21-6-9 SS material, Cheryl Evans for metallographic preparation and microhardness measurements, and Dave Hiromoto for tensile testing. This work was performed under the auspices of the U.S. Department of Energy by Lawrence Livermore National Laboratory under Contract DE-AC52-07NA27344. This document was prepared as an account of work sponsored by an agency of the United States government. Neither the United States government nor Lawrence Livermore National Security, LLC, nor any of their employees make any warranty, expressed or implied, or assume any legal liability or responsibility for the accuracy, completeness, or usefulness of any information, apparatus, product, or process disclosed, or represent that its use would not infringe privately owned rights. Reference herein to any specific commercial product, process, or service by trade name, trademark, manufacturer, or otherwise does not necessarily constitute or imply its endorsement, recommendation, or favoring by the United States government or Lawrence Livermore National Security, LLC. The views and opinions of authors expressed herein do not necessarily state or reflect those of the United States government or Lawrence Livermore National Security, LLC, and shall not be used for advertising or product endorsement purposes.

AVAILABILITY AND REQUIREMENTS OF SOFTWARE

MIDAS is a web-based application developed at Lawrence Livermore National Laboratory that allows users to assess and explore material strength models and their associated parameters, in comparison to experimental data. The application is available via the web, and access is controlled through an account setup and authentication process. Additional information can be found at: <https://pls.llnl.gov/people/divisions/physics-division/condensed-matter-science-section/eos-and-materials-theory-group/projects/midas-material-implementation-database-and-analysis-source>.

AUTHOR CONTRIBUTIONS

JWE coordinated welding, microstructure characterization, tensile testing, and performed characterization of the electron beam. GFE provided program management guidance and engineering analysis of the work performed. JNF performed MIDAS modeling of the tensile test results; IVG performed nanoindentation hardness testing; and RPM performed EBSD characterization of the base metal and welds.

COMPETING INTERESTS

The authors declare that they have no competing interests.

REFERENCES

1. D.J. Alexander, and C.T. Necker: Los Alamos National Laboratory Report, LA-UR-11-02857, 2011.
2. M.E. Kassner, and R. Breithaup: Lawrence Livermore National Laboratory Report, UCRL-89779, 1983.
3. David. Tabor: *The Hardness of Metals*, Oxford University Press, Oxford, UK, 1951.
4. S.R. Kalidindi and S. Pathak: *Acta Met.*, 2008, vol. 56, p. 3523.
5. D.J. Steinberg, S.G. Cochran, and M.W. Guinan: *J. Appl. Phys.*, 1980, vol. 51, p. 1498.
6. G.R. Johnson, and W.H. Cook: *Proceedings of the 7th International Symposium on Ballistics*, 1983, The Hague, Netherlands, p. 541.
7. J.W. Elmer and T.W. Eagar: *Weld. J.*, 1990, vol. 69 (4), pp. 141-s–150-s.
8. J.W. Elmer and A.T. Teruya: *Weld. J.*, 2001, vol. 80 (12), p. 288-s.
9. W.C. Oliver and G.M. Pharr: *J. Mater. Res.*, 1992, vol. 7 (06), pp. 1564–83.
10. J.W. Elmer, S.M. Allen, and T.W. Eagar: *Metall. Mater. Trans. A*, 1989, vol. 20A (10), p. 2117.
11. Aerospace Structural Materials Handbook, vol. 1 Ferrous Alloys, Battelle Columbus Division, 1987.
12. D. Peckner and I.M. Bernstein: *Handbook of Stainless Steels*, McGraw Hill, New York, NY, 1977.
13. C. Hills and H. Rack: *Mater. Sci. Eng.*, 1981, vol. 51, p. 231.
14. D.J. Steinberg, Lawrence Livermore National Laboratory Report, UCRL-MA-106439, 1991.
15. M. Tang, P. Norquist, N. Barton, K. Durrenberger, J. Florando, and A. Attia: Lawrence Livermore National Laboratory Report, LLNL-PROC-464065, 2010.
16. M. LeBlanc: Lawrence Livermore National Laboratory Report, ERD12-500013-AA, 2012.